Contrib Mineral Petrol (2002) 142: 501–514
DOI 10.1007/s00410-001-0310-0

Jörg Renner · Brian Evans · Greg Hirth

Grain growth and inclusion formation in partially molten carbonate rocks

Received: 14 February 2001 / Accepted: 28 August 2001 / Published online: 1 November 2001

Abstract To learn more about the kinetics and mechanisms of coarsening and melt inclusion formation, we investigated the effects of melt content, viscosity, and topology on the microstructural evolution of partially molten and melt-free calcite aggregates. Synthetic marbles with eutectic melts were produced by annealing mixtures of calcite and either calcium hydroxide or lithium carbonate for up to 80 h at a confining pressure of 300 MPa and temperatures of 973–1,023 K. The melts produced in the two systems are expected to differ significantly in viscosity. Generally, coarsening rates decrease with increasing melt fraction, probably because the diffusion length across melt pockets increases. Analysis of grain shapes in the samples with about 40% melt indicated that coarsening was accommodated by agglomeration in the samples of the calcium/lithium carbonate system. In the calcium carbonate/hydroxide system, classical Ostwald ripening occurred. For melt contents about 10% and below, melt-filled pores are either dropped from or dragged along with migrating grain boundaries, depending on the pore size and the grain boundary curvature. These data can be used to constrain the conditions where fluid or melt inclusions form under natural conditions. Combining our results and previous studies illustrates a systematic relation between the grain boundary mobility in calcite aggregates and the diffusion kinetics associated with second phases residing on the grain boundaries. In particular, boundaries with no porosity are most mobile, those boundaries dragging melt-filled pores are slower, those with gas-filled pores are slower yet, and those containing solid phases are slowest or may even be motionless.

J. Renner
Department of Earth, Atmospheric,
and Planetary Sciences,
Massachusetts Institute of Technology,
Cambridge, MA 02139, USA

B. Evans (✉)
Department of Earth, Atmospheric,
and Planetary Sciences,
Massachusetts Institute of Technology,
Cambridge, MA 02139, USA
E-mail: brievans@mit.edu
Tel.: +1-617-2532856
Fax: +1-617-2580620

G. Hirth
Department of Geology and Geophysics,
Woods Hole Oceanographic Institution,
MS #8 Woods Hole, MA 02543-1541, USA

Editorial responsibility: T.L. Grove

Introduction

The processes of grain coarsening, grain growth, and recrystallization influence, and are influenced by, the morphology of the fluid phase. Further, pores filled with gas, melts, or aqueous fluids may be included in the minerals during coarsening of the grain structure. Often, these inclusions are a link to past conditions experienced by rocks, and investigating fluid inclusions provides important information on the thermodynamic state during metamorphism (Hollister and Crawford 1981; Schiano and Bourdon 1999). The fluid phase included might also be a melt because partial melting is common in a variety of tectonic units, including oceanic ridges, island arcs, the lower continental crust, and the upper continental mantle (Wyllie 1988; Peacock 1993; Thompson and Connolly 1995). Thus, understanding the kinetics of grain growth and grain boundary mobility in the presence of fluids and melts is an important step in deciphering the history of rocks (ch. 17, in Roedder 1984).

Experiments in synthetic polycrystalline aggregates of peridotite and mid-ocean ridge basalt indicate that the growth of the olivine crystals is effectively inhibited by the presence of as little as 1 to 3 wt% melt (Hirth and Kohlstedt 1995; Faul 2000). By contrast, the presence of aqueous fluid phases are observed to promote grain growth in calcite, olivine, and quartz (Tullis and Yund 1982; Covey-Crump and Rutter 1989; Karato 1989; Hirth and Kohlstedt 1995; Covey-Crump 1997). Here

we report the results of a series of experiments in which we investigated the coarsening of solid calcite in the presence of eutectic melts of the binary systems $CaCO_3 + Li_2CO_3$ and $CaCO_3 + Ca(OH)_2$. By employing these simple systems we could vary the melt content at a given temperature without changing the melt or the solid composition. In addition, the two eutectic melts are expected to have significantly different melt viscosity, and therefore, the components of the solid grains may have different self-diffusion coefficients in each melt.

Background

Ripening in a liquid phase

When solid particles with a range of grain sizes are dispersed throughout a melt, the average grain size will increase over time by a process called Ostwald ripening, provided that the solid is soluble in the fluid (Wagner 1961; Voorhees 1992). This coarsening is driven by differences in chemical potential of solid particles with different sizes (Greenwood 1956): the smaller the grain or more convex the interface curvature, the higher the solubility of the solid in the liquid (Thompson–Freundlich equation). As a result, small particles shrink, while large particles grow. For dilute dispersions of particles, the classical theory makes two important predictions (Wagner 1961). First, distinct distributions of particle size exist in steady-state that are characteristic of transport controlled by diffusion or surface reaction. Both distributions exhibit a rather sharp cut-off at particle sizes about 1.5 times the average size. Second, the average particle size, d, is related to time by

$$\langle d\rangle^n - \langle d_0\rangle^n = k \cdot t \quad (1)$$

where d_0 is the average starting particle size at $t = 0$; k is a temperature dependent reaction constant, such that $k = k_0 \cdot \exp(-Q/RT)$ where k_o is a constant, Q is an activation energy, R is the gas constant, and T is the absolute temperature. When kinetics are controlled by the diffusion of the solid's constituents through the fluid, the growth exponent, n, is 3; $n = 2$ is expected when the kinetics are dominated by surface reactions. By using the bracket notation, we emphasize that a simple arithmetic average will, in most cases, be inadequate to characterize grain size distributions.

When the solid particles are not well-dispersed, e.g., the volume fraction of the solid phase becomes significant, two effects can cause the coarsening kinetics to deviate from the classical theory. First, the concentrations of solute in the liquid between the particles differ from the classical theory if particles are not well-dispersed. Second, physical motion may cause two or more particles to encounter each other. Modifications of the classical theory to account for changes in the diffusion geometry and/or the concentration field have been made (Jayanth and Nash 1989; Kailasam et al. 1999), but describing the interaction during encounters is more difficult. During an encounter, the rate at which the particles grow may change discontinuously owing to elevated diffusion rates (Davies et al. 1980), or because two or more particles physically contact each other (Takajo et al. 1984). Physical contact (agglomeration) is controlled by particle movement because of gravity and Brownian motion and by the duration and stability of the contact formed between the particles (Niemi et al. 1980; Courtney 1984; Shaw and Duncombe 1991).

Whether agglomeration leads to coalescence, i.e., the formation of a single grain, depends on the mobility of the newly formed grain boundary. In theory, the boundary in a two-particle agglomerate can migrate out of the agglomerate only if the angle formed at the junction of the grain boundary with the solid–liquid interface, i.e., the dihedral angle, θ, is in excess of about 45° (Zhao et al. 1998). In practice, agglomeration of multiple particles (as expected in situations with high solid content, i.e., in excess of 50 vol%) might allow for coalescence in more wetting systems.

The modified theories still predict that $(d)^3 \propto t$, provided that diffusion through the liquid controls the coarsening and that d is much larger than d_0 (Brailsford and Wynblatt 1979; Davies et al. 1980; Takajo et al. 1984; Tokuyama and Kawasaki 1984; Voorhees and Glicksman 1984; Jayanth and Nash 1989; Voorhees 1992). Although the coarsening kinetics of the classical and modified theories are similar, the development of microstructure predicted by the two sets of theories differ. Both sets of theories predict steady-state grain-size distributions. Thus, the kinetics are fully described by the behavior of the average size, but the different theories predict different distributions and effects of the solid content. In general, distributions are expected to be wider and more symmetrical than the classical predictions. The theoretical treatment of direct encounters by Takajo et al. (1984) yields symmetrical distributions independent of solid content as long as the contribution by classical Ostwald ripening is negligible. The distributions derived by Davies et al. (1980) for coarsening dominated by diffusional encounters exhibit systematically diminishing skewness with increasing solid content. The predicted distributions evolve from the classical distribution at vanishingly small solid content to a symmetric distribution when no fluid is left. With increasing solid content, distributions also become less peaked. Because the mechanism by which two particles become a single grain does not explicitly enter the statistical calculations by Takajo et al. (1984) and Davies et al. (1980), the predictions are applicable to situations controlled by encounters, by agglomeration, or by a combination of both mechanisms.

Grain growth with fluid-filled porosity

For solid contents > 80 vol%, coarsening is controlled by grain boundary mobility. If the fluid is not perfectly wetting, then the liquid phase may be characterized either as a connected pore space, or as unconnected, but

saturated, porosity. In those cases, the increase of grain size is more appropriately addressed as grain growth where the boundary mobility is limited by the motion of the fluid-filled porosity. Grain growth is also described by Eq. (1), but the growth exponents vary between 2 and 5 and cannot be interpreted uniquely (e.g., Brook 1976; Atkinson 1988; Evans et al. 2001).

Depending on kinetics parameters, the boundary velocity may be limited by the mobility of the second phases (including liquid-filled porosity; Yan et al. 1977). Mobile pores may be dragged by the moving boundary, whereas immobile pores may pin the boundary. In the latter case, if the boundary experiences a sufficiently high driving force, it may drop immobile pores and move with the intrinsic mobility between successive obstacles (Brook 1976; Hsueh et al. 1982; Spears and Evans 1982; Evans et al. 2001).

The first approximate determination of the mobility of gas- or liquid-filled pores was developed for the migration of spherical pores in a temperature gradient (Shewmon 1964). The mobility of individual spherical pores, M_p, rapidly decreases with increasing pore radius, a; $M_p \propto a^{-4}$ for diffusion of the solid's constituents along the pore's surface; $M_p \propto a^{-3}$ for diffusion through the pore fluid volume (Brook 1976). Solutions for the variation of pore mobility with dihedral angle are available for transport by pore surface diffusion (Hsueh et al. 1982; Spears and Evans 1982; Svoboda and Riedel 1992; Riedel and Svoboda 1993). As dihedral angle decreases, the diffusion path length decreases, and, consequently, pore mobility for a non-spherical pore increases by a factor of 2 to 3 compared with a spherical pore of the same cross-sectional radius (Svoboda and Riedel 1992). When the pore volume is fixed, pore mobility decreases with decreasing dihedral angle.

In geologic situations, aqueous pore fluids or melts are often present; and these may provide fast diffusion pathways. However, for the case of transport limited by diffusion through the pore, mobilities are known only for the two extreme pore shapes, spheres ($\theta \equiv 180°$; Brook 1976) and films ($\theta \equiv 0°$; Yan et al. 1977; Annavarapu et al. 1992). Intuitively, when diffusion through the fluid controls the kinetics, one expects a decrease in dihedral angle to enhance pore mobility because the diffusion path length tends to decrease. However, predictions for polycrystalline aggregates are particularly difficult because the balance between the effects of pore radius, pore/film thickness, and dihedral angle depend on the number of pores and their actual distribution.

Recently, German and Olevsky (1998) combined theories of Ostwald ripening and normal grain growth to describe coarsening in aggregates with less than about 50% melt. The growth law derived has an exponent of 3 and grain-size distributions that are well-described by Rayleigh distributions. However, there might be complications owing to the interaction between grain boundaries and fluid-filled pores. In fact, Kailasam et al. (1999) observed a growth exponent of 4 for a volume fraction of solid >0.9, which is in apparent disagreement with the combined theories.

Materials and methods

Sample preparation and experimental procedure

Starting powders were prepared by mixing reagent-grade powders of calcium carbonate ($CaCO_3$) and calcium hydroxide [$Ca(OH)_2$], or $CaCO_3$ and lithium carbonate (Li_2CO_3). To calculate the melt content at temperature requires knowledge of the mixture chemistry, the eutectic temperature, and its change with increasing pressure. The phase relation data for the two binary systems (Eitel and Skaliks 1929; Wyllie and Tuttle 1960; Wyllie and Raynor 1965; see also Fig. 1) indicate that at ambient pressure, the eutectic temperature, T_e, of both systems is about 930 to 940 K. For the $CaCO_3 + Ca(OH)_2$ system, T_e decreases by less than 10 K for an increase of pressure by 500 MPa. We used differential thermal analysis to estimate melting temperature at a pressure of 300 MPa. Estimates for both systems agreed with the room pressure data (Fig. 1); in detail, a small negative value of $\partial T_e/\partial P$ is indicated for the $CaCO_3 + Li_2CO_3$ system. Thus, we relied on the ambient-pressure phase diagrams (Fig. 1) to determine melt contents for a given powder mixture. We added 1.7, 5, and 22 wt% of $Ca(OH)_2$ or Li_2CO_3 to obtain melt contents of about 3, 10, and 40 wt% at 973 K, respectively (Table 1). Weighing errors result in an uncertainty of less than ± 0.1 wt% melt. The density of carbonatite melts is not well known. It could not be constrained by our experiments because the melts could not be quenched as glasses, but crystallized to fine-grained end-member mixtures. Thus, we quote melt contents

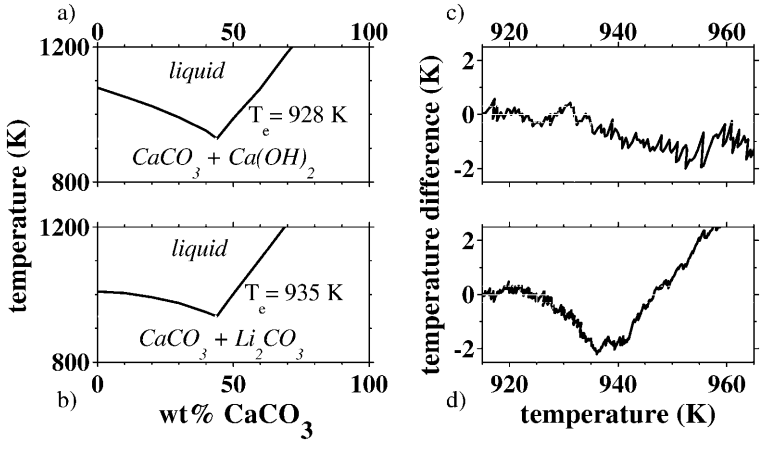

Fig. 1 Phase diagrams for **a** $CaCO_3 + CaOH_2$ (Wyllie and Tuttle 1960; Wyllie and Raynor 1965) and **b** $CaCO_3 + Li_2CO_3$ (Eitel and Skaliks 1929). **c–d** Difference in temperature between set-point temperature and actual temperature with constant power input to furnace for the two systems. The eutectic temperature at 300 MPa confining pressure is indicated by a decrease of the actual temperature from the set point

in wt% rather than vol%. In any event, the density is likely to be greater than 2,000 kg/m^3. With this lower limit, weight percentages of 3, 10, and 40 wt% correspond to volume percentages of 4, 13, and 47 vol%, respectively. According to the phase diagrams an increase in temperature from 973 to 1,023 K results in an increase of 0.4, 1.0, and 4.1 wt% for the weight percentages of 3, 10, and 40 wt%, respectively.

Samples were fabricated from the powders by a three-step process. First, the mixtures were die-pressed into copper shells at room temperature with an axial pressure of about 150 MPa. Second, the die-pressed bodies and their shells were sealed with copper end-caps, loaded into a gas vessel and hot-isostatically pressed at 973 K and 300 MPa for 5 min (Table 2). Finally, the densified aggregates were removed from the vessel and cut into discs 2–3 mm thick, without removing the copper shell. Each disc was individually enclosed with copper end-caps. Stacks of five to seven such discs, each with different composition, were then heat-treated in ten experiments (Table 3). The sample porosity after die-pressing ranged between 15 and 20%. Hot-pressed samples had densities close to that of fully dense mixtures of the solid components.

Heat-treatment

The stacked discs were heat-treated at either 973 or 1,023 K and 300 MPa, for periods between 30 min and about 80 h. To begin an experiment, the vessel was pressurized to about 220 MPa before heating commenced at a rate of about 20 K/min. The pressure increased during the heating and needed only a little adjustment (less than 10 MPa) to reach 300 MPa at the end of heating. Two different heating procedures were used for the preparatory HIPs (Table 2). Initially, we applied a two-step heating ramp with a slope of 20 K/min up to 890 K, followed by a 6 K/min ramp to the final temperature of 973 K. This procedure limited overshoot of the final temperature to less than 2 K for a period of less than a minute. A second set of samples was prepared applying only the faster rate up to the final temperature. For these samples, the overshoot was about 5 K during the first minute. The times listed in Table 3 are the total elapsed times at the final conditions. Two experiments (C-260 and C-261) were performed following a different protocol. In these control runs, two die-pressed samples, separated by copper end caps, were held at temperature for 45 min and 2 h 55 min, respectively. These experiments differed from the others in that there was not a separate HIP step, i.e., the die-pressed bodies were not densified, cooled and depressurized, cut into discs, and then pressurized and reheated.

During the heat-treatment, furnace power was controlled using a thermocouple inside the furnace, rather than the sample thermocouple touching the top of the sample through bores in the ceramic pistons. Appropriate temperature profiles were determined by repeatedly performing furnace calibrations using a bored alumina cylinder to replace the sample. To compare actual runs with the calibration profiles, the profile above the sample was determined by moving the sample thermocouple during individual experiments. Based on the calibrations, we estimate that the temperature along a sample did not vary by more than 2 K during the heat-treatment. The precision of the temperature measurement was probably within 1 K. Pt–Rh thermocouples were used, except in one evacuated run (C-306, Table 2) where a chromel–alumel thermocouple was used. In both cases, the accuracy in temperature is better than $\pm 1\%$, i.e., about ± 10 K. Cooling rates were about 60 K/min.

Table 1 Compositions and melt percentages of investigated samples

Flux	Flux (wt%)	Code[a]	Melt[b] (wt%) (@ 973/1,023 K)	Melt[c] (vol%) (@ 973/1,023 K)
$Ca(OH)_2$	1.7	H1.7	3/3.4	4/4.5
	5	H5	10/11	13/14
	22	H22	40/44	47/52
Li_2CO_3	1.7	L1.7	3/3.4	4/4.5
	5	L5	10/11	13/14
	22	L22	40/44	47/52

[a]Throughout the paper we use a short code for samples prepared that consists of a letter representing the flux (*H*: $Ca(OH)_2$; *L*: Li_2CO_3) followed by a number indicating the weight percentage of the flux

[b]The weight percentages of melt were calculated according to the phase diagrams given in Fig. 1

[c]The volume percentages of melt were approximated using a lower limit of 2 g/cm^3 for the density of the carbonatite melts

Microstructural analysis

After the heat treatment, polished sections were investigated in reflected light, and images of the majority of samples were taken with the SEM. In a few cases, thin sections were prepared. We characterized grain size by measuring the intercept length, $l_i = d_i$, (total line length divided by the number of intercepts); by compiling chord length statistics, which gives additional information about the statistical distributions of grain size in 2-D; and by determining perimeter statistics yielding shortest and longest axis, and diameter of circle with equivalent area as the grain. In all cases, at least 500 grains were measured. Size distributions obtained from the perimeter analysis are represented by the first moment (the expectation value, d) and the square root of the second moment (the standard variation, $\sigma = sqrt\langle d^2 \rangle$; Table 3). We determined normalized $\int_0^\infty g_{(u)} du = 1$ distributions $g_{(u)}$ of the ratio $u = d/\langle d \rangle$ to compare results from experiments at different conditions.

Physical properties of carbonatite melts

Viscosities of carbonatite melts are generally low (not too different from water!) and exhibit only moderate temperature and pressure dependence (Treiman and Schedl 1983; Wolff 1994; Dobson et al. 1996). There are no direct measurements for the two binary systems we used, but the viscosity of binary carbonate systems seems to vary linearly with composition between the end member values. Applying such a simple rule of mixture to the experimentally determined viscosity of Li_2CO_3 melt (Janz et al. 1964) and the inferred viscosity of $CaCO_3$ melt (Wolff 1994) suggests a viscosity of about 10^{-1} to 10^{-2} Pas for the $CaCO_3 + Li_2CO_3$ eutectic melt at 1,000 K. Based on the differences between melt viscosities of Na and K carbonates and hydroxides (Janz et al. 1964; Klemm 1964), we estimate the viscosity of the $CaCO_3 + Ca(OH)_2$ eutectic melt to be at least ten times lower than that of the $CaCO_3 + Li_2CO_3$ eutectic melt.

We determined dihedral angles from SEM microphotographs (10,000×) of samples containing 10% melt that were synthesized at 973 and 1,023 K for 78 and 20 h, respectively. For each sample, 150 angles were measured in a connected area, with an accuracy of $\pm 2°$. For the four samples investigated, angles between about 5 and 200 are most frequent, with a suggestion that the angles are slightly lower in the $CaCO_3 + Li_2CO_3$ system than the $CaCO_3 + Ca(OH)_2$ system (Fig. 2). In addition, for both systems, the dihedral angle increases slightly with temperature.

As with any measurement made after an experiment, there is a possibility that the dihedral angles changed during cooling. There are, however, two arguments based on the structures observed after cooling that provide bounds on the microstructure actually present at the run conditions. First, in both the Ca–Li carbonate system and the calcium hydroxide–carbonate system, the presence of melt inclusions in the grains of samples with 40 wt% melt (Fig. 3C, F) indicate an early stage of agglomeration. Thus, the dihedral angles are probably larger than zero. Second, the inwardly curved shapes of inclusions in these high melt content experiments on the Ca–Li carbonate system mimic the shapes of the triple junction structures

Table 2 Conditions and results of the preparatory hot isostatic pressing (HIP) runs

Run	Composition	T (K)	$d_{i,0}$[a] (μm)	(d_0)[b] (μm)	χ[c]
C-265	H5	975[d]	29		
C-266	L1.7	974[d]	33		
C-269	L5	976[d]	32	48 ± 24	1.76 ± 0.53
C-270	H1.7	971[d]	36		
C-271	Pure	975[d]	7		
C-302	H5	971[e]	23		
C-303	L5	972[e]	28		
C-304	L1.7	970[e]	29		
C-305	H1.7	972[e]	31	46 ± 19	1.50 ± 0.44
C-306	Pure	973[e]	21[f]		
C-307	L22	969[e]	–	40 ± 12	1.61 ± 0.40
C-309	H22	970[e]	–	22 ± 7	1.37 ± 0.26

[a]Intercept values
[b]Expectation values with standard deviations of the diameter of a circle that has an area equivalent to a given grain (perimeter analysis)
[c]Aspect ratios (long axis/short axis) with standard deviation (perimeter analysis)
[d]Heating with two ramp rates (15 k/min up to about 890 K followed by 5 K/min until indicated temperature)
[e]Heating with a single ramp rate (15 K/min)
[f]Evacuated

Table 3 Conditions and results of the static annealing experiments. Single numbers represent line intercepts d_i; the entries in the second and third row of a cell represent expectation values (d_0) with standard deviations of the diameter of a circle with equivalent area and aspect ratios, χ (long axis/short axis), with standard deviation, respectively. The pure samples labeled ev were evacuated during HIP (i.e., came from HIP C-306 (see Table 2)

Run	T (K)	Time (s)	Pure	H1.7	H5	H22	L1.7	L5	L22
C-260	972	45 min					53	47	
C-261	975	2 h 55 min		84	72				
C-275	978	23 h 31 min	32	100	100		195	133	
C-276	1,032	2 h	9	45	52		44	41	
C-277	1,028	19 h 32 min	39	120	94		155	101	
C-279	980	2 h 6 min	12	55	53		74	76	
C-308	1,022	2 h	12	63	51		76	62	
C-311	974	30 min	19ev	44	41	32 ± 11 1.26 ± 0.18	45	42	46 ± 13 1.59 ± 0.38
C-312	972	78 h 7 min		132	120	104 ± 40 1.36 ± 0.39	165	141 142 ± 68 1.67 ± 0.56	123 ± 49 1.52 ± 0.36
C-313	973	7 h 3 min	17ev	102 111 ± 63 1.66 ± 0.64	72 73 ± 32 1.50 ± 0.44	58 ± 21 *1.27 ± 0.18*	107 67 ± 51 1.66 ± 0.48	94 85 ± 61 1.71 ± 0.56	71 ± 25 1.53 ± 0.33
C-314	1,022	30 min		47	44 45 ± 20 1.59 ± 0.47	36 ± 12 1.29 ± 0.20	58	46 48 ± 19 1.56 ± 0.38	52 ± 18 1.59 ± 0.42
C-315	1,021	7 h 2 min		117 113 ± 70 1.53 ± 0.45	85 83 ± 34 1.48 ± 0.42	68 ± 22 1.28 ± 0.21	151 162 ± 74 1.60 ± 0.39	103 104 ± 50 1.62 ± 0.46	86 ± 32 1.47 ± 0.30

found in the samples with less melt. The presence of these convex inclusions indicates that the dihedral angles present during the experiment were below 60° (Fig. 3F).

Results

Average grain size

The ripening and growth data show five general trends (see Table 3, Fig. 4). First, all partially molten samples contain larger average grain size than the pure, i.e. melt-free, reference samples. Second, the average grain size of partially molten samples decreases with increasing melt content. Third, samples with $CaCO_3 + Li_2CO_3$ melt exhibit slightly larger grains than samples containing $CaCO_3 + Ca(OH)_2$ melt for all experimental conditions. Fourth, an increase in temperature promotes growth. Finally, the reproducibility is fair (for example, compare C-276 to C-308). Differences between samples after nominally identical experiments are larger for the $CaCO_3 + Li_2CO_3$ than for the

$CaCO_3 + Ca(OH)_2$ system. In the samples with melt, the results obtained from discs prepared with a preparatory HIP run are consistent with those from the control runs (C-260 and C-261) that did not have a separate HIP step.

Evacuation of the sample assembly during pressurization and heating has a large effect on the grain size in pure samples. Sample C-306 was evacuated during heating and reached a grain size three times larger than sample C-271. The main difference between the two is that the pore space of C-271 was initially filled with air (Table 2). However, when sample C-306 was cooled and depressurized, and then pressurized and reheated without evacuation, the growth rate decreased. We argue below that the introduction of gas-filled pores during subsequent steps of depressurization, cooling, re-pressurization, and re-heating, results in a decrease in growth rate in the melt-free samples.

Analyzing the data in terms of the growth law [Eq. (1)] reveals that the growth exponent, n, ranges between 3 and 6 and depends on melt composition as well as melt content. Growth exponents for samples with 3 and 10 wt% $CaCO_3 + Ca(OH)_2$ melt are between 4 and 5 (Fig. 4), whereas samples with 40 wt% melt are well described by an exponent of 4 over the entire range of conditions. For the $CaCO_3 + Li_2CO_3$ system, n is between 3 and 4 for samples with 3 and 10 wt% melt, except at longer times when growth rates decay. By contrast, the samples with 40 wt% melt show a steady increase in growth rate, with exponents decreasing from 5 to 3 for long experiments. The effect of temperature is roughly consistent with an apparent activation energy $Q = -nR\partial \ln d/\partial(1/T)$ between 100 to 200 kJ/mole for all melt contents and compositions, but the thermal activation of the coarsening process is obscured by the increase of melt content with temperature.

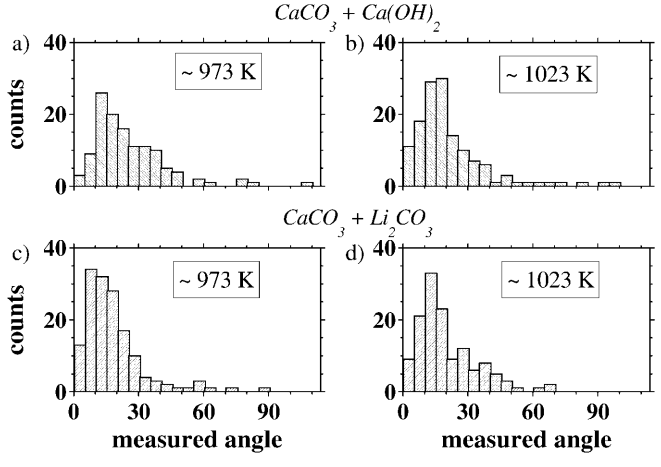

Fig. 2 Distribution of dihedral angles observed between two neighboring grains in two-dimensional section for samples with 5 wt% of $CaOH_2$ (**A** and **B**) and Li_2CO_3 (**C** and **D**) annealed at 973 and 1,023 K. The most frequent angle represents the dihedral angle

Grain-size and melt distributions

By characterizing the grain-size distribution we can determine the validity of the grain growth law [Eq. (1)]. It is often assumed that a simple proportionality factor (about 1.5) exists between a mean intercept length determined in two-dimensions, and the grain size in three dimensions. However, such a simple relation holds only if the grains are nearly isometric or ellipsoidal with random shape orientation (Underwood 1970). The perimeter analysis revealed that, independent of melt content and composition, grains are slightly elongated with aspect ratios between 1.2 and 1.6 (Table 3), although a preferred shape orientation does not exist. The average intercept length and the diameter of the circle with equivalent area are similar (Table 3), and their distributions are also comparable. In fact, all distributions show a steep increase to a peak in number density at sizes below the average, i.e., the mode is less than the average (Fig. 5); and the size distributions smoothly tail-off towards multiples of the mode. Such distributions can be represented by a log-normal distribution,

$$f_{\ln(d)} = 1/(\sqrt{2\pi}\ln\sigma)\cdot\exp\left\{-\left[(\ln d - \ln\langle d\rangle)/(\sqrt{2}\ln\sigma)\right]^2\right\},$$

or a Rayleigh distribution,

$$f_{R(d)} = d\cdot\ln(4)\cdot\exp\left[\ln(0.5)\cdot d^2\right]$$

Note, that the width of the distributions varies with time, melt content, and composition (Fig. 6).

In samples with 40 wt% $CaCO_3 + Ca(OH)_2$ melt, the grains reached a nominally steady state distribution after about 30 min at 973 K (Fig. 6A). This distribution is considerably wider than that observed for samples heated for 5 min at temperature. In contrast, at the same conditions, distributions in the $CaCO_3 + Li_2CO_3$ system show only small changes for annealing times up to 7 h, but the entire distribution broadens considerably when samples are heated for 78 h (Fig. 6B). For a given elapsed time and temperature, the width of the distribution gradually increases with decreasing melt content for the $CaCO_3 + Ca(OH)_2$ system (Fig. 6C). But, in the $CaCO_3 + Li_2CO_3$ system, distributions for samples with 3 and 10 wt% melt do not differ significantly and have substantial tails towards high sizes that are not observed in the sample with 40 wt% melt (Fig. 6D).

Unlike grain size, the melt distribution differs significantly for the two systems. Independent of the content of $CaCO_3 + Ca(OH)_2$ melt, grains with moderate size variations are either homogeneously dispersed in the melt (Fig. 3A–C) or in contact with melt residing in triple junction pools that also show moderate size variation (Fig. 7A–B). In contrast, grains in samples with 40 wt% $CaCO_3 + Li_2CO_3$ melt tend to agglomerate. The skeletal structure that results is slowly removed with increasing time, leaving homogeneously dispersed, but odd-shaped, particles behind (Fig. 3D–F). In

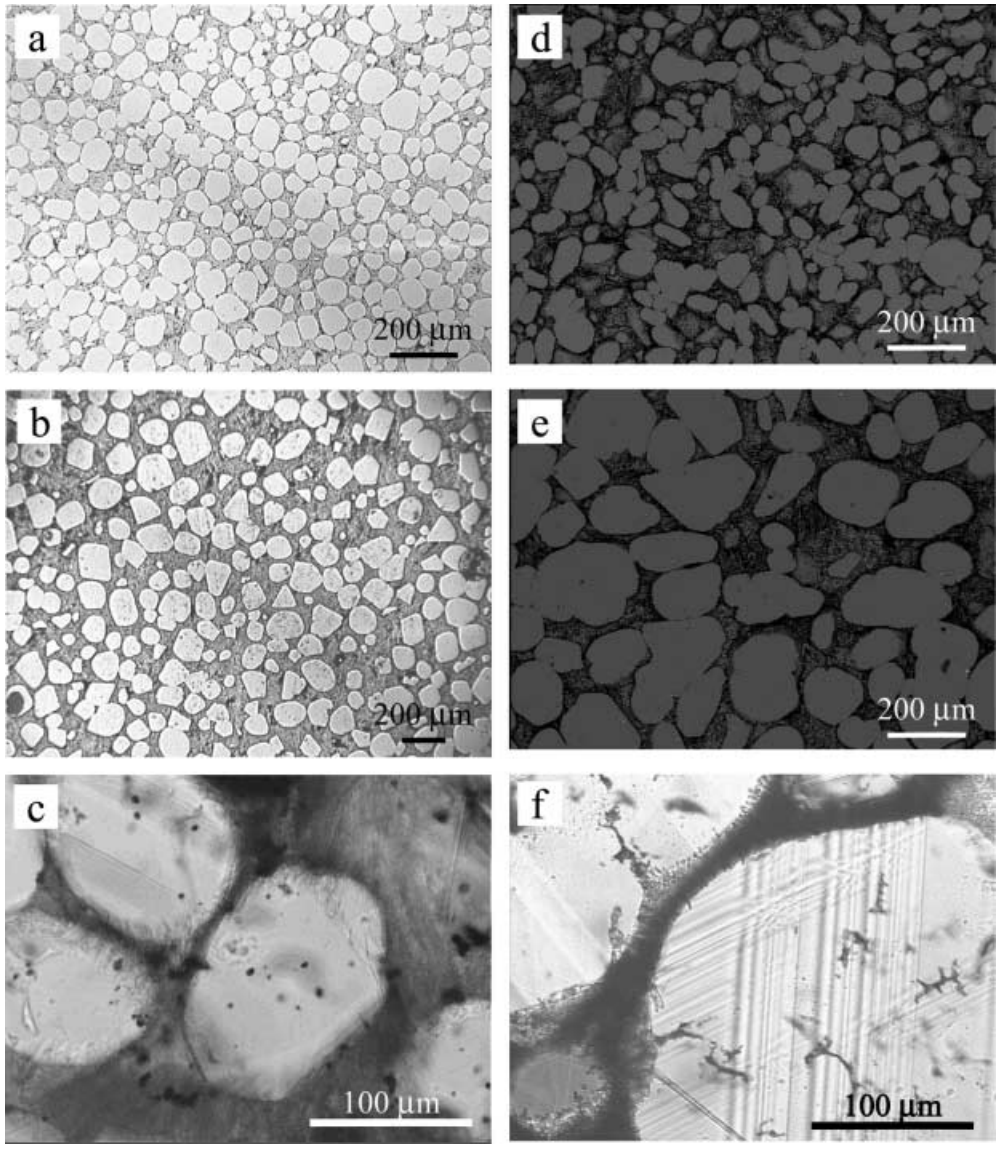

Fig. 3 Microstructures of samples with 40 wt% melt after 7 and 78 h of annealing at a temperature of 973 K. **a–c** $Ca(OH)_2$ flux. **d–f** Li_2CO_3 flux. **a** After 7 h. **b, c** After 78 h annealing. **a, b** Reflected light. **c** Transmitted light. Isometric particles of nearly spherical shape are homogeneously distributed in the melt and vary modestly in size. **a** and **b** were taken at different magnifications to emphasize that the grain-size distribution does not vary with annealing time. **c** The particles are free of grain boundaries and contain mostly spherical inclusions. **d** SEM micrograph of sample after 7 h of heat-treatment. **E** After 78 h annealing. **f** Transmitted light micrograph after 78 h. Particles tend to agglomerate causing a skeletal structure (**d**) that is slowly removed with increasing annealing time, leaving more homogeneously dispersed, but oddly shaped particles behind (**e**). **f** Despite the presence of abundant inclusions that preserve the shape of triple junctions and document the agglomeration history, the grains are free of grain boundaries

samples with lower melt content, large grains are surrounded by others that are an order of magnitude smaller (Fig. 7C–D). In addition, the melt gathers into large pools.

Melt inclusions are observed in grains in both systems. In samples with large fractions of $CaCO_3 + Li_2CO_3$ melt, the shape of inclusions is similar to that observed at triple grain junctions in samples with small fractions of melt, suggesting that they formed as a result of agglomeration. Despite the shape of these inclusions, and the odd, often serrated, shapes of the solid particles themselves, the calcite grains are actually single crystals (Fig. 3F). In samples with high contents of $CaCO_3 + Ca(OH)_2$ melt, inclusions are less abundant and nearly spherical (Fig. 3C). At lower melt contents, there are also fewer inclusions present in samples with the $CaCO_3 + Ca(OH)_2$ melt; small melt inclusions (1 to 2 μm) occur only in clusters in the grain interiors (Fig. 8A). In samples with $CaCO_3 + Li_2CO_3$ melt, inclusions with sizes down to the limit of optical resolution are frequent in the grain interiors, even near grain boundaries (Fig. 8B). For both systems, inclusions in excess of 10 μm are found in the largest grains (Fig. 7). Also, large melt pockets on the boundaries are often distorted, possibly by grain boundary drag.

Discussion

Ostwald ripening and grain growth are both coarsening processes driven by reduction of interface energy. Traditionally, coarsening of solid grains embedded in a large amount of fluid is treated as ripening, whereas coarsening in the presence of only a few percent of fluid is considered to be grain growth. In the discussion below we maintain the distinction, although the separation is largely heuristic because both processes must be identical at intermediate fluid contents.

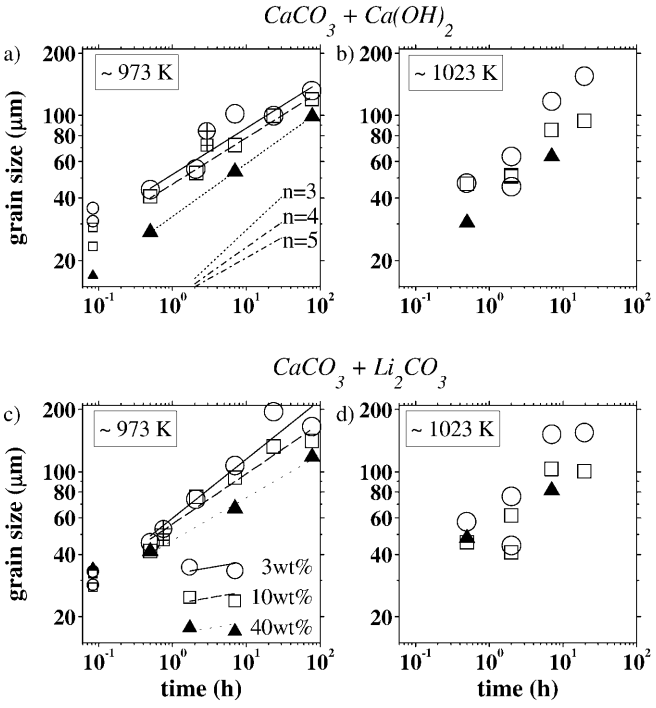

Fig. 4 Coarsening behavior of calcite grains in contact with melt fluxed by $Ca(OH)_2$ (**a** and **b**) and by Li_2CO_3 (**c** and **d**) at 973 and 1,023 K (see Tables 2 and 3). Line intercept values are plotted for the low melt content samples (1.7 and 5 wt% flux added). The expectation values for the diameter of a sphere with equivalent area, as obtained from perimeter analysis, are plotted for the high-melt content samples (40 wt% melt). The small *symbols* represent the preparatory HIPs (Table 2); the *crossed symbols* represent the control runs C-260 and C-261 (see Table 3). Because the grain size after annealing exceeds the grain size of the preparatory HIPs in all cases the initial grain size term in Eq. (1) can be neglected and the growth behavior can be analyzed by comparing the slopes with those corresponding to growth exponents between 3 and 5. *Trend lines* are shown to emphasize the differences owing to variation in melt content (**a** and **c**). It is important to note that the growth exponent may actually change as a function of time

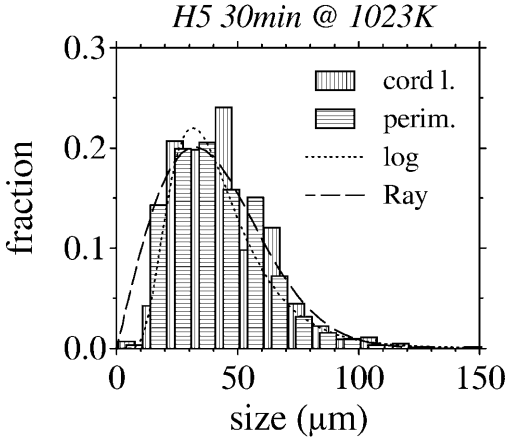

Fig. 5 Grain-size distributions gained from cord length and perimeter analyses do not differ significantly and are consistent with either a log-normal distribution or a Rayleigh distribution (see text for formulae)

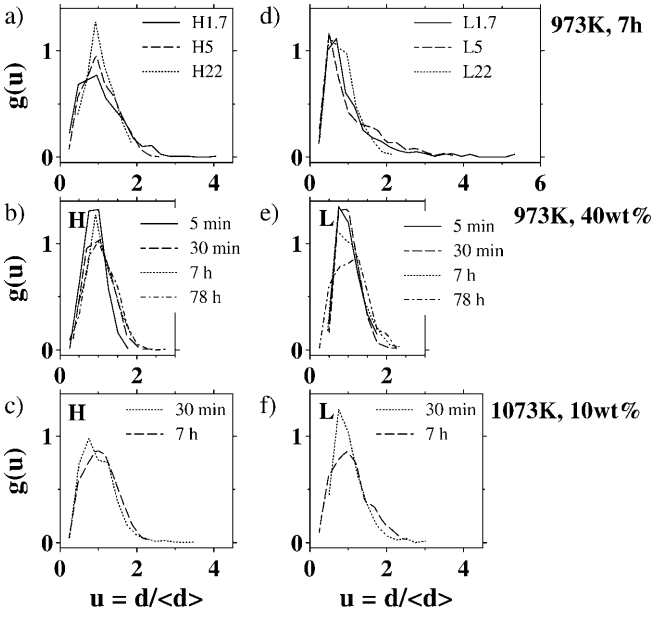

Fig. 6 Normalized size distributions as a function of melt content, annealing time, and temperature for the (**a–c**) $CaCO_3 + Ca(OH)_2$ system and the (**d–f**) $CaCO_3 + Li_2CO_3$ system. **A** At given annealing time and temperature (7 h and 973 K), the distribution width gradually increases with decreasing melt content. **b** The grains apparently reach a steady-state distribution at a melt content of 40 wt% and temperatures of 973 and 1,023 K after 30 min annealing. **c** Grain-size distributions are not affected much by annealing time at a temperature of 1,023 K and a melt content of 10 wt%. **d** The distributions for the two samples with the lower melt content (3 and 10 wt%) are similar and have substantial tails towards high sizes. **e** At a melt content of 40 wt% and a temperature of 973 K the distributions show only modest changes at the high size end for annealing times up to 7 h, whereas after 78 h, the entire distribution broadens considerably. **f** Grain-size distributions do not seem to reach steady state at a temperature of 1,023 K and a melt content of 10 wt% for annealing times up to 7 h

For large melt contents, in both the calcium hydroxide-carbonate and Ca–Li carbonate systems, the growth exponents exceed 2, indicating that the rate of coarsening is not limited by a surface reaction, but, rather, that it is controlled by diffusion in the melt. In this case, the rate constant, k, should be proportional to the coefficient for self-diffusion through the melt of the slowest constituent of the solid phase, and to the concentration of the solute in the fluid. The exponent for grain growth is not as diagnostic of the mechanism as it is for Ostwald ripening. If the grain boundary mobility is controlled by the drag of fluid-filled pores, the growth constant, k, is proportional to the concentration and diffusivity of the rate-limiting solid constituent in the fluid, as is also true in the case of ripening.

Data for self-diffusion coefficients in these melts do not exist. However, one may estimate relative diffusion rates by comparing melt viscosities because self-diffusion rates generally increase with decreasing melt viscosity. For example, the self-diffusion rates of calcium, aluminum, and oxygen in molten $CaO–Al_2O_3–SiO_2$ scale with an inverse fractional power of the viscosity (Liang et al. 1996), but those authors note that the coefficients do not

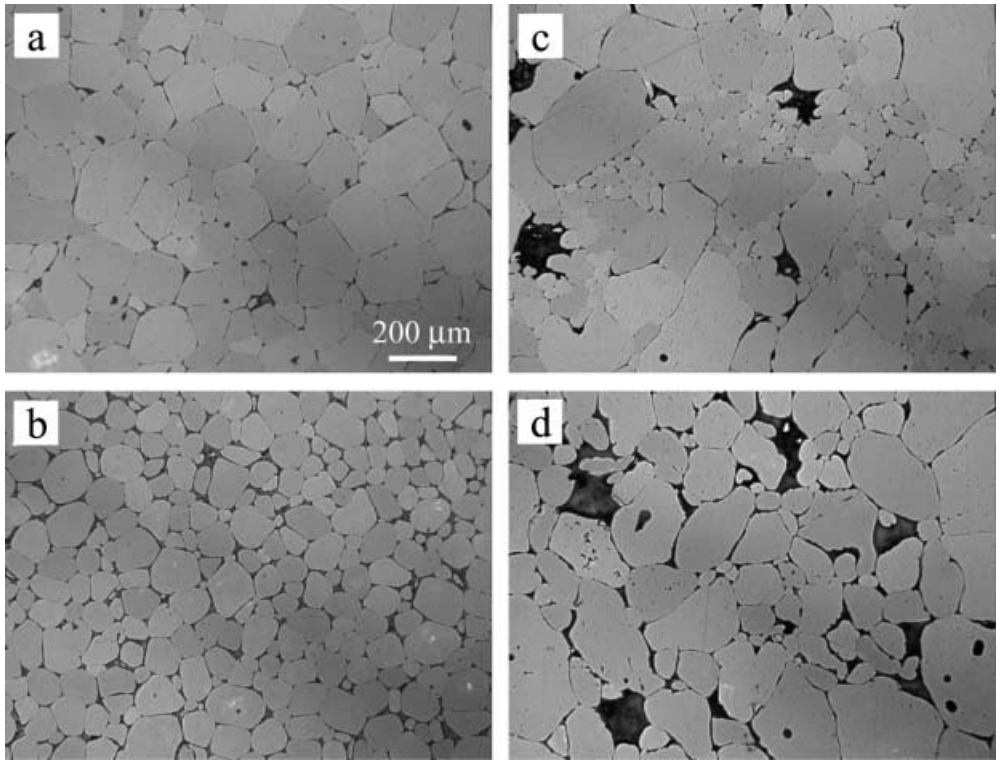

Fig. 7 Microstructures of samples after 7 h annealing at a temperature of 973 K (*scale bar* applies to all microphotographs). **a** 1.7 wt% $Ca(OH)_2$; **b** 5 wt% $Ca(OH)_2$: grains of near spherical shape and triple junction melt pockets are homogeneously distributed and vary moderately in size. **c** 1.7 wt% Li_2CO_3; **d** 5 wt% Li_2CO_3: very large grains are surrounded by grains that are smaller by one order of magnitude or more. In addition, melt is gathered in large pools. For both systems, inclusions of remarkable size (in excess of 10 μm) and distorted pores indicating drag are found in or around the largest grains

obey simple Stokes–Einstein or Eyring equations. Self-diffusion data for molten alkali carbonates (Spedding and Mills 1965), and predictions for pure $CaCO_3$ melt based on molecular dynamics simulations (Genge et al. 1995) also lend support to this approach for carbonatite melts. Thus, based on analogy with other alkali carbonate and hydroxide systems, one would expect the viscosity of the Ca-hydroxide system to be lower, perhaps much lower than the Ca–Li carbonate system. If self-diffusion rates in the two systems do actually differ, then an explanation of the similarity in coarsening rates is necessary. Further, the melt-free samples grow the slowest. How can these observations be reconciled with theories for grain growth and coarsening?

In the following discussion, we assume that observations taken from two-dimensional sections accurately portray the evolution of microstructure in three dimensions and that microstructure observed in the quenched state represents that characteristic of the run conditions. Because grain shape anisotropy is involved, it is cumbersome, if not impossible, to relate 2-D and 3-D distributions (Underwood 1970). Thus, some of the tailing-off at large grain sizes (e.g., Fig. 6) might be exaggerated owing to stereographic effects. This problem is important because under some circumstances the growth exponent can differ substantially for analyses in two and three dimensions (Rhines and Craig 1974; Atkinson 1988). Fortunately, the Rayleigh distribution, which seems to represent our data well, also has the special property of being invariant to changes in dimensionality (Louat 1974).

Mechanisms of ripening in samples with 40 wt% melt

Two microstructural features suggest that different processes dominate coarsening in the two systems, even though the overall rates are similar. First, the two systems exhibit significant differences in the shape of the melt–solid interfaces. The perimeters of grains in the Ca–Li carbonate system are often serrated, suggesting that smaller grains coalesced (Fig. 3E). By contrast, grains in the calcium hydroxide–carbonate system seldom have serrated boundaries; most are smooth and gently curved (Fig. 3B). Similarly, melt inclusions in the Ca–Li carbonate system often resemble triple junctions (Fig. 3F), whereas inclusions in samples fluxed with calcium hydroxide are mostly round (Fig. 3C). The process that leads to the removal of the serrated interfaces is analogous to neck growth (Courtney 1977), most likely controlled by diffusion through the liquid because the coalesced aggregates are free of grain boundaries. Second, the tendency for grains in the Ca–Li carbonate system to form a skeletal structure is consistent with slower diffusion in a higher viscosity melt. Agglomeration is controlled by the mobility of the grains in the melt, and the likelihood that two approaching grains make contact before the smaller one dissolves. Although a lower viscosity enhances the mobility of particles in the melt, the chances of actual contact are actually reduced because Ostwald ripening is enhanced (Niemi et al. 1980; Courtney 1984).

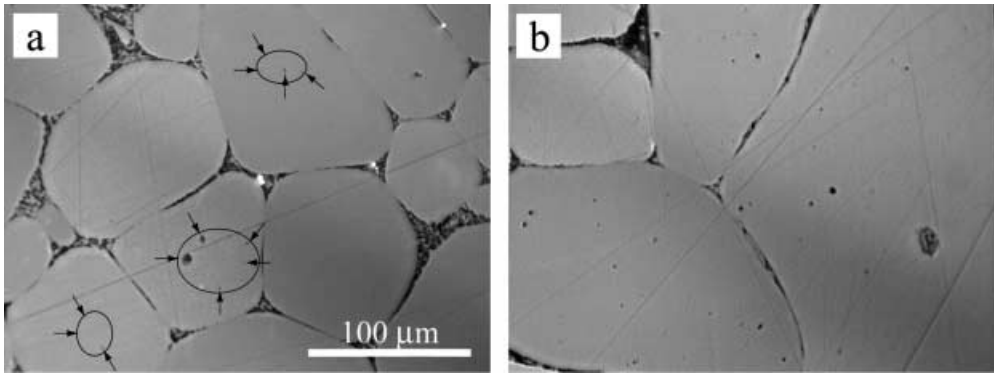

Fig. 8 Photomicrograph in reflected light of samples with 5 wt% flux after 7 h of annealing at a temperature of 973 K (*scale bar* applies to both microphotographs). **a** With $Ca(OH)_2$ flux, the melt inclusions (*arrows*) are clustered in the grain centers. The microstructure indicates a switch from pore drag to pore drop. The absence of pores outside the cluster suggests that pores of the sizes found in the cluster are dragged once the grain size is approximately equal to the size of the cluster. **b** In the Li_2CO_3 system, the melt inclusions are distributed throughout the grains and must have been dropped for all grain sizes. The smallest pores near to a grain boundary provide a bound on the size of pores that cannot be dragged

Based on these observations we suggest that agglomeration with subsequent coalescence is the dominant coarsening mechanism in the Ca–Li carbonate system, a supposition consistent with comparatively slower diffusion kinetics in this melt. After considerable coarsening, the coalescence frequency decreases because the inter-particle spacing increases. A different growth process results for calcite grains in melt fluxed by calcium hydroxide, perhaps owing to faster diffusion kinetics. Then, enhanced mass transport occurs when small grains encounter larger grains, inhibiting coalescence. Steady-state grain-size distributions are achieved relatively quickly. These results are consistent with modified Ostwald ripening theories.

Grain growth in samples with low melt content

The distribution of melt inclusions in the samples with 3 and 10 wt% melt provides evidence for a difference in the growth process related to differences in diffusion kinetics. As illustrated in Fig. 8A, the melt inclusions are clustered near the centers of the grains in the hydroxide system. These inclusions were probably dropped from migrating grain boundaries during the initial phase of the experiment. A zero-order estimate of the condition for pore-boundary separation (drop) can be derived in terms of a critical pore radius (Hsueh et al. 1982)

$$a_c^m \geq f_{(d/a,\theta)} \frac{\Omega^{1/3} D \gamma_{sl}}{k_B T M_b \gamma_b}$$

where f denotes a function of the grain/pore size ratio and the dihedral angle, Ω and D the atomic volume and the diffusion coefficient of the diffusing species, respectively, k_B is Boltzmann's constant, T is the absolute temperature, M_b the mobility of the boundary, and γ_{sl} and γ_b the solid–liquid interface and the boundary energy, respectively. The exponent m is 2 for surface diffusion (with $D = D_s \cdot \delta_s$, where δ_s is the surface width) and 1 for diffusion through the liquid.

By measuring the inclusion sizes and estimating the grain size at the time the inclusions formed, we can constrain conditions where pores are dragged or dropped by a migrating boundary (Fig. 9). Because there is substantial uncertainty in the grain size and because the variation in grain size is not large, we plot the drag/drop criterion as a vertical line, although the critical pore size

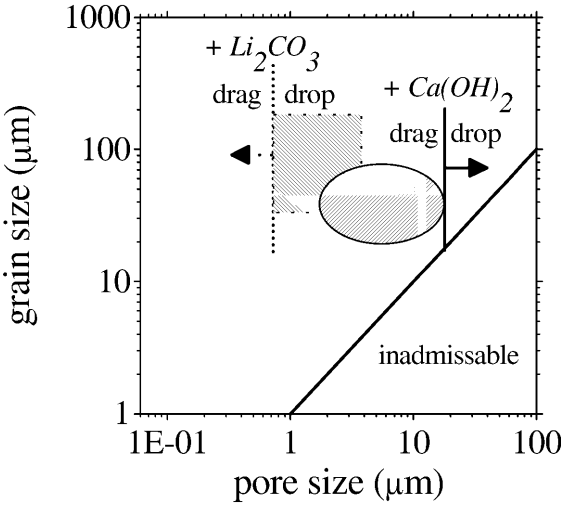

Fig. 9 Conditions for drag and drop of melt-filled pores in a grain-size/pore-size diagram. For the calcium hydroxide–carbonate system we evaluated pore and cluster size. More than 50 measurements are represented by the *shaded ellipse*. For the Ca–Li carbonate system, where the pores are being dropped, more than 100 measurements are represented by the *shaded rectangle*. Because there is considerable uncertainty in the data, we did not attempt to evaluate the slope of the relation between the pore size and the grain size. Thus, the drag–drop relations are plotted as *vertical lines*, even though it is clear that the critical pore size depends on grain size. Pores in the calcium hydroxide–carbonate system that are ten times larger than those in the Ca–Li carbonate system, are still mobile enough to be dragged. The higher pore mobility in the former system indicates faster self-diffusion rates

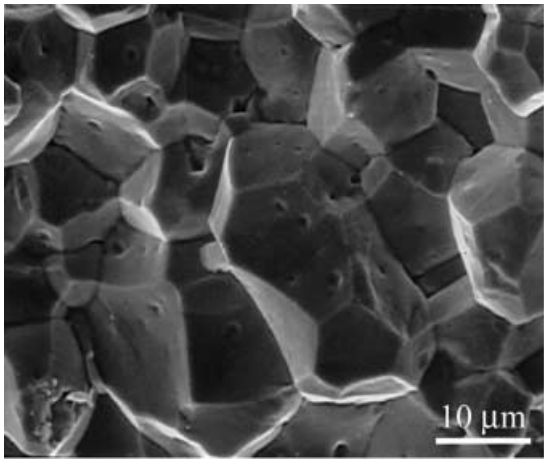

Fig. 10 SEM microphotograph of melt-free sample (C-306) hot-pressed after evacuation. Some pores still reside on two-grain boundaries and triple junctions

must depend on the velocity (and hence, curvature) of the migrating grain boundary (Hsueh et al. 1982). Conversely, melt inclusions are found everywhere in the grains of the Ca–Li carbonate system, even in close proximity to grain boundaries. These inclusions provide an upper bound estimate of the size that may be dragged by the boundaries. Because the amount of melt in the experiments was fixed, and because intergranular melt pockets exhibit similar dihedral angles, the conditions for pore drag and drop are controlled by the mobility of the melt filled pores, which in turn is controlled by diffusion through the melt. Fast diffusion increases the pore mobility and, therefore, shifts the boundary towards larger pore sizes, as found for the calcium hydroxide–carbonate system.

Judging from the microstructure in samples with a low content of Ca–Li carbonate melt (Fig. 8A), we suppose that grain boundaries initially migrate with a high intrinsic mobility after dropping even very small melt pores. However, the high growth rates probably cannot be maintained and decrease when grains reach a size that requires the drag of the melt-filled pores. This decay of abnormal growth results in stagnation of the increase in average grain size (Fig. 4).

Several observations demonstrate the intimate relation between growth and ripening for the range in melt fraction explored here. For Ca–Li carbonate samples, the initial agglomeration results in a microstructure characterized by two features: areas with less than 5 vol% melt, and melt pools with sizes controlled by the absolute melt content. The coalescence step in the samples with 40 wt% melt is, therefore, likely the same process that accommodates abnormal growth observed for samples with 3 and 10 wt% melt. The modest effect of melt content on the initial growth rate (Fig. 4) is consistent with the observation that the grain-scale melt topology is independent of melt content. It is possible that topological descriptions of pore drag need to be modified for cases when more than two grains agglomerate. When the agglomeration geometry is complex, the variability of curvature at the contacts, of the grain sizes, and of the surface energy might relax

Fig. 11 Grain growth in calcite rocks at a temperature of 973 K. All but one of the data sets are for synthetic calcite rocks. Differences in total and fluid pressures result only in second order effects (see Covey-Crump 1997). A slope corresponding to a growth exponent of $n=3$ is given by the *fine dashed line*. Data from this study are for pure melt-free samples with (*closed circle*) and without (*open circle*) evacuation, and for samples with 3 wt% melt (*solid and long dashed line*). Note that we report only intercept lengths, thus, the data of this study may differ from other reports by a factor of 1.5. Sources: *R84* (Rutter 1984) synthetic calcite with added water; *C-C86* (Covey-Crump 1986) synthetic calcite with added water (the *long–short dashed line* gives the fit to the data as reported by Covey-Crump 1997). *OE86* (Olgaard and Evans 1986) synthetic calcite with added alumina particles (the *box* represents the final grain sizes reached in experiments with different sizes and amounts of the alumina particles). *OE88* (Olgaard and Evans 1988) synthetic calcite (approx. 6% porosity) with added water and carbon dioxide (*open diamonds*), Solnhofen limestone (approx. 5% porosity) with added carbon dioxide showed almost no coarsening over the times explored (*shaded box*). *C-C97* (Covey-Crump 1997) synthetic calcite rock without added pore fluid (*short–short–long dashed line*); initial growth with an exponent close to 2 does not represent steady-state conditions. Coarsening ceased between 10 and 20 h of annealing; all other rocks exhibited less coarsening. Thus the trend line shown is an upper bound

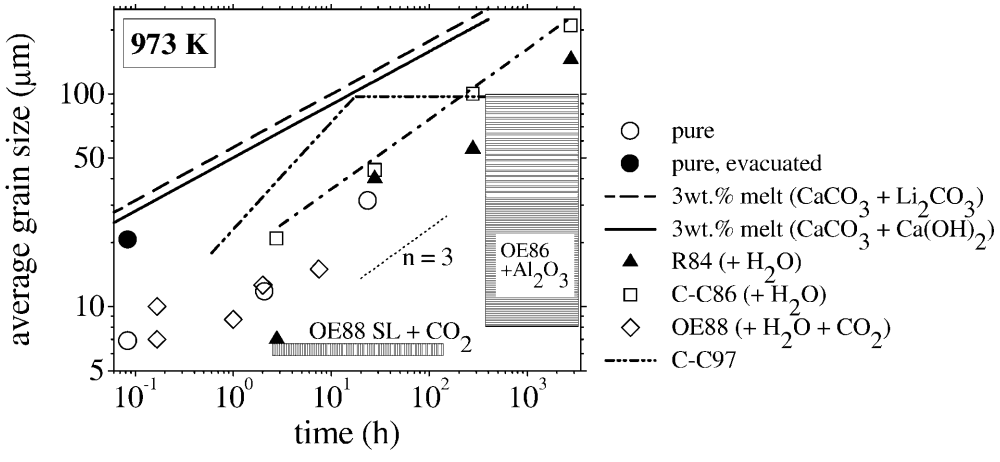

the topological constraints derived from a two-grain analysis.

In the samples fluxed by small amounts of calcium hydroxide, the grain boundaries drag pores of substantial size, limiting their mobility. Only very large melt pores are dropped to form inclusions. For the entire range in melt content we studied, steady-state grain-size distributions are achieved quickly, and the distributions broaden with decreasing melt content, in agreement with predictions of modified Ostwald ripening theories (Davies et al. 1980).

Intrinsic grain boundary mobility of calcite

The observation that samples without melt exhibit the slowest growth rates contradicts our interpretation that the intrinsic mobility of melt-free grain boundaries is high. But, SEM observations on fracture surfaces of the melt-free samples confirm the presence of a large number of pores with a diameter of about 200 nm on grain boundaries and edges (Fig . 10), and it is likely that these gas-filled pores slow grain boundary migration.

We found that melt-free samples prepared with evacuation showed no further growth after quenching and re-heating. The inhibition of growth after re-jacketing and re-heating suggests that many grain boundaries crack during the quench (owing to anisotropy in elastic and thermal properties) and that these cracks do not fully close when brought back to run conditions. The textures in these samples likely evolve in a manner analogous to healing cracks (Hickman and Evans 1987) or to the structures observed by Olgaard and FitzGerald (1993). Those authors found channels and grooves on boundaries in synthetic calcite aggregates, in addition to clusters of pores in the grain centers. The gas-filled pores produced by quenching and subsequent healing upon reheating could then poison grain growth. A similar transition from pore-drop to pore-drag was observed in gas-filled peridotite samples (Karato 1989).

A systematic relationship between the growth rate of calcite aggregates and the diffusion kinetics of secondary phases can be illustrated by comparing our results with other studies (see Fig. 11 and Olgaard and Evans 1986; Olgaard and Evans 1988; Covey-Crump 1997). Growth rates are inhibited the most by interactions between boundaries and immobile solid particles. Boundary mobility is also effectively pinned by the presence of pores filled with inert gas. Pores filled with hydrous fluids will be more mobile. The growth rate in the partially molten samples is most rapid, and for the Ca–Li carbonate system, where abnormal grain growth is observed, the boundary mobility may approach the intrinsic mobility.

Geological implication

The drag–drop criterion shown in Fig. 9 illustrates the way that textural analyses of natural rocks could be used to estimate conditions where melt inclusions form, and thus constrain melt transport processes in the crust and mantle. By combining chemical analyses with textural measurement of the size and spatial distribution of melt inclusions, such a relationship can be used to estimate the grain size in partially molten regions of the mantle, and therefore provide constraints on both the rheology and permeability of mantle aggregates. In addition, the relative order of in-situ diffusion kinetics of the constituents of gaseous fluids and melts can be estimated and compared with laboratory results.

Conclusions

We investigated the effect of annealing time, melt content, and melt viscosity on the coarsening behavior of partially molten calcite aggregates. At temperatures exceeding the melting points by less than 100 K, the average grain size increases by almost one order of magnitude in less than 100 h. When the kinetics of transport through the melt are slow, coarsening occurs by agglomeration and successive coalescence, providing that the aggregate contains 40 wt% melt. When less melt is present, abnormal growth may occur as boundaries break free of the inclusions and leave them within the matrix grains. If diffusion is faster, growth rates are controlled by the drag of more mobile pores (i.e., the grain boundaries do not break free of the melt pockets). Observations for samples containing 40 wt% melt under these conditions agree with predictions of modified theories of Ostwald ripening. We find a systematic relationship between the growth behavior of calcite aggregates and the diffusion kinetics of secondary phases. The grain boundary mobility in two-phase calcite aggregates decreases from melt to liquid to vapor to solid inclusions in the drag regime. In the drop regime, the boundary mobility presumably approaches the intrinsic mobility. Because the boundary between the two regimes is largely determined by the relative sizes of matrix grains and the secondary phases, grain growth and melt inclusion formation strongly depend on the initial geometric constraints, in addition to the diffusion kinetics.

Acknowledgements Funding was provided by National Science Foundation grants OCE9529807 (MIT) and OCE9626930 (WHOI). J.R. gratefully acknowledges support from the Alexander von Humboldt foundation. We appreciate the thorough and considered review by E.B. Watson and the comments of an anonymous reviewer. Sincere thanks to N. Chatterjee who helped with the SEM work.

References

Annavarapu S, Liu J, Doherty R (1992) Grain growth in the solid plus liquid two-phase field: instability of liquid films at migrating grain boundaries. Mater Sci Forum 94–96:649–658

Atkinson HV (1988) Theories of normal grain growth in pure single phase systems. Acta Metall 36:469–491

Brailsford AD, Wynblatt P (1979) The dependence of Ostwald ripening kinetics on particle volume fraction. Acta Metall 27:489–497

Brook RJ (1976) Controlled grain growth. In: Wang FF-Y (ed) Ceramic fabrication procedures, vol 9. Academic Press, New York, pp 331–364

Courtney TH (1977) A reanalysis of the kinetics of neck growth during liquid phase sintering. Metall Trans A Phys Metall Mater Sci 8A:671–677

Courtney TH (1984) Densification and structural development in liquid phase sintering. Metall Trans A Phys Metall Mater Sci 15A:1065–1074

Covey-Crump SJ (1986) Grain growth kinetics of calcitic aggregates. Geology. University of London, London

Covey-Crump SJ (1997) The normal grain growth behaviour of nominally pure calcitic aggregates. Contrib Mineral Petrol 129:239–254

Covey-Crump J, Rutter EH (1989) Thermally-induced grain growth of calcite marbles on Naxos Island, Greece. Contrib Mineral Petrol 101:69–86

Davies CKL, Nash P, Stevens RN (1980) The effect of volume fraction of precipitate on Ostwald ripening. Acta Metall 28:179–189

Dobson DP, Jones AP, Rabe R, Sekine T, Kurita K, Taniguchi T, Kondo T, Kato T, Shimomura O, Urakawa S (1996) In-situ measurement of viscosity and density of carbonate melts at high pressures. Earth Planet Sci Lett 143:207–215

Eitel W, Skaliks W (1929) Ueber einige Doppelcarbonate der Alkalien und Erdalkalien. Z Anorg Allgem Chem 183:263–286

Evans B, Renner J, Hirth G (2001) A few remarks on the kinetics of static grain growth in rocks. Int J Earth Sci (Geologische Rundschau) 90:88–103

Faul U (2000) Constraints on the melt distribution in anisotropic polycrystalline aggregates undergoing grain growth. In: Bagdassarov N, Laporte D, Thompson AB (eds) Physics and chemistry of partially molten rocks. Kluwer, Boston, pp 67–92

Genge MJ, Price GD, Jones AP (1995) Molecular dynamics simulations of $CaCO_3$ melts to mantle pressures and temperatures: implications for carbonatite magmas. Earth Planet Sci Lett 131:225–238

German RM, Olevsky EA (1998) Modeling grain growth dependence on the liquid content in liquid-phase-sintered materials. Metal Mater Trans 29A:3057–3067

Greenwood GW (1956) The growth of dispersed precipitates in solutions. Acta Metall 4:243–248

Hickman SH, Evans B (1987) Influence of geometry upon crack healing rate in calcite. Phys Chem Mineral 15:91–102

Hirth G, Kohlstedt DL (1995) Experimental constraints on the dynamics of the partially molten upper mantle: deformation in the diffusion creep regime. J Geophys Res 100:1981–2001

Hollister LS, Crawford ML (1981) Short course in fluid inclusions: applications to petrology. Course handbook, vol 6. Mineralogical Association of Canada, Calgary

Hsueh CH, Evans AG, Coble RL (1982) Microstructure development during final/intermediate stage sintering – I. Pore/grain boundary separation. Acta Metall 30:1269–1279

Janz GJ, Ward AT, Reeves RD (1964) Molten salt data. Rensselaer Polytechnic Institute, Troy, NY

Jayanth CS, Nash P (1989) Factors affecting particle-coarsening kinetics and size distribution. J Mater Sci 24:3041–3051

Kailasam SK, Glicksman ME, Mani SS, Fradkov VE (1999) Investigation of microstructural coarsening in Sn–Pb alloys. Metall Mater Trans A 30A:1541–1547

Karato S (1989) Grain growth kinetics in olivine aggregates. Tectonophysics 168:255–273

Klemm A (1964) Transport properties of molten salts. In: Blander M (ed) Molten salt chemistry. Interscience Publishers, New York, pp 535–606

Liang Y, Richter FM, Davis AM, Watson EB (1996) Diffusion in silicate melts; I, Self diffusion in $CaO–Al_2O_3–SiO_2$ at 1,500 °C and 1 GPa. Geochim Cosmochim Acta 60:4353–4367

Louat NP (1974) On the theory of normal grain growth. Acta Metall 22:721–724

Niemi AN, Baxa LE, Lee JK, Courtney TH (1980) Coalescence phenomena in liquid phase sintering – conditions and effects on microstructure. In: Hausner HH, Antes HW, Smith GD (eds) Modern developments in powder metallurgy. Proc 1980 Int Powder Metall Conf, vol 12. Am Powder Metall Inst, Princeton, NJ, pp 483–495

Olgaard DL, Evans B (1986) Effect of second-phase particles on grain growth in calcite. J Am Ceram Soc 69:C-272–C-277

Olgaard DL, Evans B (1988) Grain growth in synthetic marbles with added mica and water. Contrib Mineral Petrol 100:246–260

Olgaard DL, FitzGerald JD (1993) Evolution of pore microstructures during healing of grain boundaries in synthetic calcite rocks. Contrib Mineral Petrol 115:138–154

Peacock SM (1993) Large-scale hydration of the lithosphere above subducting slabs. Chem Geol 108:49–59

Rhines FN, Craig KR (1974) Mechanisms of steady-state grain growth in aluminum. Metall Trans 5:413–425

Riedel H, Svoboda J (1993) A theoretical study of grain-growth in porous solids during sintering. Acta Metall Mater 41:1929–1936

Roedder E (1984) Fluid inclusions, vol 12. Mineralogical Society of America, Washington, DC

Rutter EH (1984) The kinetics of grain coarsening in calcite rocks. Prog Exp Petrol 6:245–249

Schiano P, Bourdon B (1999) On the preservation of mantle information in ultramafic nodules; glass inclusions within minerals versus interstitial glasses. Earth Planet Sci Lett 169:173–188

Shaw TM, Duncombe PR (1991) Forces between aluminum oxide grains in a silicate melt and their effect on grain boundary wetting. J Am Ceram Soc 74:2495–2505

Shewmon PG (1964) The movement of small inclusions in solids by a temperature gradient. Trans Metall Soc AIME 230:1134–1137

Spears MA, Evans AG (1982) Microstructure development during final/intermediate stage sintering – II. Grain and pore coarsening. Acta Metall 30:1281–1289

Spedding PL, Mills R (1965) Trace-ion diffusion in molten alkali carbonates. J Electrochem Soc 112:594–599

Svoboda J, Riedel H (1992) Pore-boundary interactions and evolution equations for the porosity and the grain size during sintering. Acta Metall Mater 40:2829–2840

Takajo S, Kaysser WA, Petzow G (1984) Analysis of particle growth by coalescence during liquid phase sintering. Acta Metall 32:107–113

Thompson AB, Connolly JAD (1995) Melting of the continental crust; some thermal and petrological constraints on anatexis in continental collision zones and other tectonic settings. J Geophys Res 100:15565–15579

Tokuyama M, Kawasaki K (1984) Statistical-mechanical theory of coarsening of spherical droplets. Physica 123A:386–411

Treiman AH, Schedl A (1983) Properties of carbonatite magma and processes in carbonatite magma chambers. J Geol 91:437–447

Tullis J, Yund RA (1982) Grain growth kinetics of quartz and calcite aggregates. J Geol 90:301–318

Underwood EE (1970) Quantitative stereology. Addison-Wesley, Reading, MA

Voorhees PW (1992) Ostwald ripening of two-phase mixtures. Annu Rev Mater Sci 22:197–215

Voorhees PW, Glicksman ME (1984) Ostwald ripening during liquid phase sintering – effect of volume fraction on coarsening kinetics. Metall Trans A 15A:1081–1088

Wagner C (1961) Theorie der Alterung von Niederschlaegen durch Umloesen (Ostwald-Reifung). Z Elektrochemie 65:581–591

Wolff JA (1994) Physical properties of carbonatite magmas inferred from molten salt data, and application to extraction patterns

from carbonatite–silicate magma chambers. Geol Mag 131: 145–153
Wyllie PJ (1988) Magma genesis, plate tectonics, and chemical differentiation of the Earth. Rev Geophys 26:370–404
Wyllie PJ, Raynor EJ (1965) DTA and quenching methods in the system $CaO–CO_2–H_2O$. Am Mineral 50:2077–2082
Wyllie PJ, Tuttle OF (1960) The system $CaO–CO_2–H_2O$ and the origin of carbonatites. J Petrol 1:1–46
Yan MF, Cannon RM, Bowen HK (1977) Grain boundary migration in ceramics. In: Fulrath RM, Pask JA (eds) Ceramic microstructures. Westview Press, Boulder, pp 276–307
Zhao J, Ikuhara Y, Sakuma T (1998) Grain growth of silica-added zirconia annealed in the cubic/tetragonal two-phase region. J Am Ceram Soc 81:2087–2092